

## Improving the lead adsorption performance of mesoporous MnO<sub>2</sub> by plasma surface modification

Haipeng Zhang<sup>a,b</sup>, Yanju Yang<sup>b</sup>, Limin Yuan<sup>c</sup>, Guodong Liu<sup>a</sup>, Yuhua Shan<sup>b</sup>,  
Xiaoqing Qian<sup>b</sup>, Juanjuan Wang<sup>b,\*</sup>

<sup>a</sup>Jiangsu Key Laboratory of Crop Genetics and Physiology, Jiangsu Co-Innovation Center for Modern Production Technology of Grain Crops, Yangzhou University, Yangzhou 225009, China, emails: hpzhang@yzu.edu.cn (H.P. Zhang), 006874@yzu.edu.cn (G.D. Liu)

<sup>b</sup>College of Environmental Science and Engineering, Yangzhou University, Yangzhou 225009, China, Tel. +86-514-87979528; Fax: +86-514-87978626; emails: wangjuanjuan@yzu.edu.cn (J.J. Wang), yangyanju@yzu.edu.cn (Y.J. Yang), shanyuhua@outlook.com (Y.H. Shan), qianxq@yzu.edu.cn (X.Q. Qian)

<sup>c</sup>Testing Center of Yangzhou University, Yangzhou 225009, China, email: lmyuan@yzu.edu.cn (L.M. Yuan)

Received 8 May 2019; Accepted 3 February 2020

### ABSTRACT

In this work, ordered mesoporous MnO<sub>2</sub> for the adsorptive removal of Pb(II) from aqueous solutions was prepared using KIT-6 silica as a template, followed by plasma modification. For comparison, a bulk MnO<sub>2</sub> adsorbent with the same crystal structure was also prepared by thermal decomposition. The MnO<sub>2</sub> adsorbents were characterized using X-ray diffraction, transmission electron microscopy, X-ray photoelectron spectroscopy, and N<sub>2</sub> adsorption–desorption measurements. The characterization results showed that plasma modification did not affect the porous structure of mesoporous MnO<sub>2</sub>, but resulted in an increased number of surface hydroxyl groups. The results of adsorption experiments showed that plasma-modified mesoporous MnO<sub>2</sub> exhibited a significantly higher Pb(II) adsorption capacity than bulk MnO<sub>2</sub>. The adsorption kinetics of Pb(II) onto the modified MnO<sub>2</sub> was best described by a pseudo-second-order kinetic model. Moreover, enhanced Pb(II) adsorption was observed at higher solution pH and in the presence of coexisting Na<sup>+</sup> and Ca<sup>2+</sup> ions. Regeneration experiments confirmed that the modified MnO<sub>2</sub> could be effectively recycled. In conclusion, plasma-modified mesoporous MnO<sub>2</sub> could be used as a recyclable adsorbent for the effective removal of Pb(II) from aqueous solutions.

*Keywords:* Manganese oxide; Plasma modification; Adsorption isotherms; Heavy metal pollutants

### 1. Introduction

Water contamination by high Pb(II) concentrations is raising global concerns, as lead is one of the most toxic heavy metals for humans [1]. Traces of Pb(II) can cause cancer and have other harmful health effects when accumulated in the human body [2]. The US Environmental Protection Agency limits the maximum Pb(II) concentration in wastewater to 0.05 mg L<sup>-1</sup>. To date, considerable efforts have been made to develop techniques for removing Pb(II) from wastewater,

including chemical precipitation, ion exchange, adsorption, and reverse osmosis [3,4]. Due to its easy operation and high efficiency, adsorption is one of the most promising and widely used approaches for Pb(II) removal from wastewater.

Ubiquitous manganese oxides are extensively utilized as adsorbents for the removal of Pb(II) from wastewater, due to their competitive cost and high adsorption affinity for metal ions. Wang et al. [5] found that layered MnO<sub>2</sub> adsorbents with low isoelectric points have high adsorption capacities for the removal of Pb(II) from acidic solutions. He and Xie [6] prepared hydrous manganese oxide and found that this adsorbent exhibits high adsorption capacities for heavy metal

\* Corresponding author.

ions. Manganese oxides with different morphologies, such as a tube, sheet, rod, sphere, and porous structures, possess a variety of specific surface areas and available surface adsorption sites that affect the Pb(II) adsorption capacity [4,7–9]. In particular, Zhang et al. [10] demonstrated that the adsorption capacities of MnO<sub>2</sub> adsorbents for Pb(II) are highly correlated with their morphology and structure. Hence, it has been proposed that manganese oxides with larger specific surface areas have higher adsorption capacity for Pb(II).

In the past decade, mesoporous materials (e.g., SiO<sub>2</sub> and carbon) have attracted widespread interest in wastewater treatment due to their ordered mesostructure, high surface area, and large pore volume [11–13]. Wang et al. [14] found that SBA-15 mesostructured silica exhibited high adsorption affinity for different heavy metal ions, such as Cu<sup>2+</sup>, Zn<sup>2+</sup>, and Ni<sup>2+</sup>. Yang et al. [15] reported that ordered mesoporous carbon CMK-3 showed high adsorption capacities and good diffusion properties as potential adsorbents for the removal of pollutants in water. Moreover, these hierarchical structures have been found to promote mass transfer and the generation of active sites, enabling the effective adsorption of Pb(II). Mesoporous manganese oxides have been successfully prepared and widely applied in many fields, such as lithium-ion batteries [16], supercapacitors [17], and catalysts [18]. Mesoporous MnO<sub>2</sub> is usually prepared using nanocasting methods with mesoporous SiO<sub>2</sub> or carbon structures as a template [19,20]. To produce mesoporous MnO<sub>2</sub>, the final products need to be heated to a high temperature (>350°C) to maintain their hierarchical structure during the template removal. Unfortunately, the heating procedure can substantially reduce the number of active adsorption sites (e.g., hydroxyl groups) on the adsorbent surface and therefore decrease the adsorption capacity of m-MnO<sub>2</sub> [21]. Plasma treatment is an effective technique to generate large amounts of active adsorption sites on the channel surfaces of mesoporous materials [22–25]. It has been speculated that plasma-modified mesoporous MnO<sub>2</sub> could be used as an efficient Pb(II) adsorbent with high adsorption capacity for wastewater treatment. However, only a few studies have been published on this subject.

In this paper, we employ plasma treatment to modify the surface of mesoporous MnO<sub>2</sub> to increase its Pb(II) adsorption capacity. We report the synthesis of plasma-modified mesoporous MnO<sub>2</sub> using mesoporous SiO<sub>2</sub> (KIT-6) as a hard template. For comparison, an additional adsorbent based on bulk MnO<sub>2</sub> nanoparticles was prepared by thermal decomposition. The results show that plasma-modified mesoporous MnO<sub>2</sub> can achieve both rapid Pb(II) adsorption kinetics and extraordinarily high Pb(II) adsorption capacity, highlighting the promising potential of the modified mesoporous MnO<sub>2</sub> as an effective adsorbent for the removal of Pb(II) from wastewater.

## 2. Experimental

### 2.1. Materials and reagents

All chemical reagents were of analytical grade. Triblock copolymer P123 ( $M_w = 5,800$ ) and humic acid were purchased from Sigma-Aldrich (St. Louis, USA). Manganese nitrate hexahydrate (Mn(NO<sub>3</sub>)<sub>2</sub>·6H<sub>2</sub>O, >98% purity) was obtained

from Alfa Aesar (Ward Hill, USA). Tetraethyl silicate, n-butanol, lead nitrate (Pb(NO<sub>3</sub>)<sub>2</sub>), sodium nitrate (NaNO<sub>3</sub>), calcium nitrate (Ca(NO<sub>3</sub>)<sub>2</sub>), sodium hydroxide (NaOH), ethanol, and hydrochloric acid (HCl) were purchased from Nanjing Chemical Reagents Co., Ltd. (Nanjing, China). Stock solutions of inorganic salts were prepared by dissolving appropriate amounts of NaNO<sub>3</sub>, Ca(NO<sub>3</sub>)<sub>2</sub>, and Pb(NO<sub>3</sub>)<sub>2</sub> in deionized water.

### 2.2. Adsorbent preparation and modification

Mesoporous MnO<sub>2</sub> was prepared as described in previous studies [19,20], using mesoporous SiO<sub>2</sub> (KIT-6) as a template. Briefly, 12 g of Mn(NO<sub>3</sub>)<sub>2</sub>·6H<sub>2</sub>O was dissolved in 50 mL of ethanol under fast stirring; then, 4 g of KIT-6 was added to the solution and ultrasonically dispersed for 30 min. The mixture was magnetically stirred for 6 h and heated at 200°C for 3 h. The above impregnation step was repeated two more times. Finally, the sample was heated in an oven at 450°C for 3 h. The mesoporous MnO<sub>2</sub> sample, denoted as m-MnO<sub>2</sub>, was obtained by removing the KIT-6 template using a 2 mol L<sup>-1</sup> NaOH solution at room temperature followed by filtration, washing, drying at 105°C for 12 h, and heating at 450°C for 3 h.

Plasma-modified mesoporous MnO<sub>2</sub> was prepared following a previously reported procedure [22]. The plasma system consisted of a high-voltage generator (CTP-2000K, Nanjing Suman, Nanjing, China) and a quartz reaction chamber. One gram of m-MnO<sub>2</sub> powder was spread in the reaction chamber to form a thin layer. Under O<sub>2</sub> flow (40 mL min<sup>-1</sup>) at normal pressure, the m-MnO<sub>2</sub> powder was treated for 30 min with an output power of 90 W. The material obtained from the plasma treatment is denoted as p-MnO<sub>2</sub>. As a control sample, bulk MnO<sub>2</sub> was prepared by heating Mn(NO<sub>3</sub>)<sub>2</sub>·6H<sub>2</sub>O at 450°C for 3 h. The obtained bulk MnO<sub>2</sub> is denoted as t-MnO<sub>2</sub>.

### 2.3. Adsorbent characterization

Small-angle X-ray diffraction (XRD) patterns were recorded on a D/max-RA powder diffractometer (Rigaku, Tokyo, Japan) equipped with a Cu K<sub>α</sub> radiation source operating at 40 kV and 40 mA, in the 2θ range of 0.8–8°. Wide-angle XRD patterns were collected in the 2θ range of 10–80°. The morphologies of the adsorbents were inspected by transmission electron microscopy (TEM; H-800, Hitachi, Tokyo, Japan) and field-emission scanning electron microscope (FESEM; S-4800II, Hitachi, Tokyo, Japan), and energy dispersive spectrometer microscope detection to observe the composition. Fourier transform infrared spectroscopy spectra were collected with KBr pellet with an IRPrestige-21 instrument (FT-IR, Shimadzu, Kyoto, Japan) with a wavelength range of 400–4,000 cm<sup>-1</sup>. The Brunauer–Emmett–Teller surface areas and pore size distributions of the adsorbents were determined by N<sub>2</sub> adsorption–desorption measurements on an ASAP 2020 porosimetry analyzer (Micromeritics, Norcross, USA) at –196°C. The chemical states of the Mn and O elements in the adsorbents were analyzed by X-ray photoelectron spectroscopy (XPS) on a PHI5000 VersaProbe system (ULVAC-PHI, Kanagawa, Japan) equipped with a monochromatized Al K<sub>α</sub> excitation source (hν = 1486.6 eV). The C 1s peak (284.6 eV) was used for the calibration of the binding

energy values. The zeta potentials of m-MnO<sub>2</sub> and p-MnO<sub>2</sub> were performed to evaluate the pH influence on the surface charge. The experiments were done for m-MnO<sub>2</sub> and p-MnO<sub>2</sub> within a pH range of 1–10 using 0.1 mol L<sup>-1</sup> NaOH or HNO<sub>3</sub> to adjust the desired pH value.

#### 2.4. Batch adsorption experiments

The adsorption of Pb(II) onto the adsorbents was investigated using a batch equilibrium technique [10]. Twenty milligrams of adsorbent was introduced in a 50 mL glass-stopped conical flask containing 40 mL of Pb(II) solution, with initial concentrations ranging from 5 to 70 mg L<sup>-1</sup>. The pH was adjusted to four using a 0.1 mol L<sup>-1</sup> HCl or NaOH solution before adding the adsorbent. After shaking for 24 h and filtering out solid particles, the concentration of Pb(II) in the filtrates was determined by atomic absorption spectrophotometry (AAS; model 2380, Perkin Elmer, Waltham, USA). The adsorbed amount  $q_e$  (mg g<sup>-1</sup>) of Pb(II) on the adsorbents was calculated according to Eq. (1):

$$q_e = \frac{V(C_0 - C_e)}{m} \quad (1)$$

where  $C_0$  and  $C_e$  represent the initial and equilibrium Pb(II) concentration (mg L<sup>-1</sup>), respectively,  $V$  is the volume of the solution (L), and  $m$  is the mass of added adsorbent (g).

To examine the Pb(II) adsorption kinetics, 0.25 g of m-MnO<sub>2</sub> or p-MnO<sub>2</sub> was added to 500 mL of a Pb(II) solution with a concentration of 50 mg L<sup>-1</sup>. The mixtures were then stirred in an incubator at 25°C. Sampling was carried out by fast filtration from the flask at preset time intervals during the adsorption process. The Pb(II) concentration in the filtrates was determined by AAS.

The effect of pH on the Pb(II) adsorption on p-MnO<sub>2</sub> was tested by adjusting the pH level of the Pb(II) solutions using a 0.01 mol L<sup>-1</sup> HCl or NaOH solution. The p-MnO<sub>2</sub> dosage and initial Pb(II) concentration were 20 and 50 mg L<sup>-1</sup>, respectively. After reaching the adsorption equilibrium, the mixtures were filtered and the Pb(II) concentrations determined. The influence of coexisting ions on Pb(II) adsorption was investigated by the addition of NaNO<sub>3</sub> or Ca(NO<sub>3</sub>)<sub>2</sub> solutions with different concentrations (0–0.2 mol L<sup>-1</sup>) at pH 4 and 25°C. The mixtures were then shaken for 24 h and filtered, and the Pb(II) concentrations were determined as described above. To further evaluate the adsorption selectivity of p-MnO<sub>2</sub> for Pb(II), adsorption isotherms of Pb(II) on p-MnO<sub>2</sub> were measured from batch adsorption tests with the same procedure used for Pb(II) in the presence of Cu(II), Ni(II) and Zn(II), respectively.

#### 2.5. Column adsorption tests

Column adsorption tests of the removal of heavy metal ions were carried out at 25°C using a polyethylene column (Omnifit Co., UK) with an inner diameter of 15 mm and a length of 130 mm containing p-MnO<sub>2</sub>. Three milliliters of wet p-MnO<sub>2</sub> powder (4.1 g) was packed in the column. At the top and bottom of the column, quartz sand (diameter ~0.2 mm; does not adsorb Pb(II)) was packed to prevent the loss of adsorbents and control the flow. The influent solution

containing 75 mg L<sup>-1</sup> Pb(II) was continuously pumped through the column at a rate of 60.0 mL h<sup>-1</sup> using a calibrated syringe pump (Longerpump Co., Baoding, China) for 10 h. This concentration is greater than the maximum concentration permitted by China's quality standard for groundwater (GB/T 14848-2017), which stipulates a threshold of 0.1 mg L<sup>-1</sup> for Pb(II). Effluent samples were collected regularly using a BSZ-100 fraction collector (Huxi Analysis Instrument Factory Co., Shanghai, China) and subjected to AAS.

To investigate the feasibility of p-MnO<sub>2</sub> for removing heavy metal ions from real wastewater, we collected sewage from the sewage discharge port of an electroplating factory in Yangzhou, China. The wastewater was used directly without treatment. The pH and chemical oxygen demand (COD) were 4.51 and 864.7 mg L<sup>-1</sup>, respectively. The concentrations of Pb(II) in the wastewater were 25.6 mg L<sup>-1</sup>.

#### 2.6. Desorption and regeneration experiments

The reusability of p-MnO<sub>2</sub> was tested by repeated Pb(II) adsorption and desorption for eight consecutive cycles. In each cycle, 50 mL of a 50 mg L<sup>-1</sup> Pb(II) solution was mixed with 20 mg of p-MnO<sub>2</sub> for 24 h. Desorption of saturated p-MnO<sub>2</sub> was conducted by dissolving Pb(II)-loaded p-MnO<sub>2</sub> in 40 mL of 0.1 mol L<sup>-1</sup> HCl, HNO<sub>3</sub> and H<sub>2</sub>SO<sub>4</sub> solution, respectively, at room temperature for 12 h. The p-MnO<sub>2</sub> adsorbent was then separated and washed thoroughly with deionized water until pH 7, before the next adsorption cycle.

### 3. Results and discussion

#### 3.1. Material characterization

The small-angle XRD spectra of m-MnO<sub>2</sub> and p-MnO<sub>2</sub> are shown in Fig. 1a. The XRD pattern of m-MnO<sub>2</sub> shows diffraction peaks at  $2\theta$  angles of 1.03° and 1.83°, corresponding to the (211) and (332) planes, respectively, denoting an ordered mesoporous structure with cubic Ia3d symmetry [26,27]. In the case of p-MnO<sub>2</sub>, the XRD pattern displays a strong (211) peak and a rather weak (332) signal, suggesting that the mesoporous structure was retained after plasma modification. The wide-angle XRD patterns of t-MnO<sub>2</sub>, m-MnO<sub>2</sub>, and p-MnO<sub>2</sub> are shown in Fig. 1b. Their sharp and intense diffraction peaks indicate that the MnO<sub>2</sub> adsorbents were well crystallized. The XRD patterns of all adsorbents exhibit diffraction peaks at  $2\theta$  values of 28.6°, 37.3°, 41.0°, 42.8°, 56.6°, 59.4°, 65.1°, and 72.4°, which could be indexed to the (110), (101), (200), (111), (211), (220), (002), and (112) planes, respectively [28,29]. These features indicate that the MnO<sub>2</sub> adsorbents consisted of a  $\beta$ -MnO<sub>2</sub> crystalline phase, corresponding to the rutile structure of pyrolusite [10].

The structure and morphology of the MnO<sub>2</sub> adsorbents are shown in transmission electron microscopy (TEM) images (Fig. 2). The t-MnO<sub>2</sub> sample (Fig. 2a and b) possessed a flake-like morphology with aggregated MnO<sub>2</sub> particles. The m-MnO<sub>2</sub> sample (Fig. 2c and d) had a well-ordered mesoporous structure with aligned nanorods and uniform pore dimensions. The m-MnO<sub>2</sub> pore diameter estimated from the TEM images was 10.3 nm on average, whereas the diameter of the nanorods was approximately 4.0 nm. Similarly, an ordered assembly of MnO<sub>2</sub> rods was observed for p-MnO<sub>2</sub>,

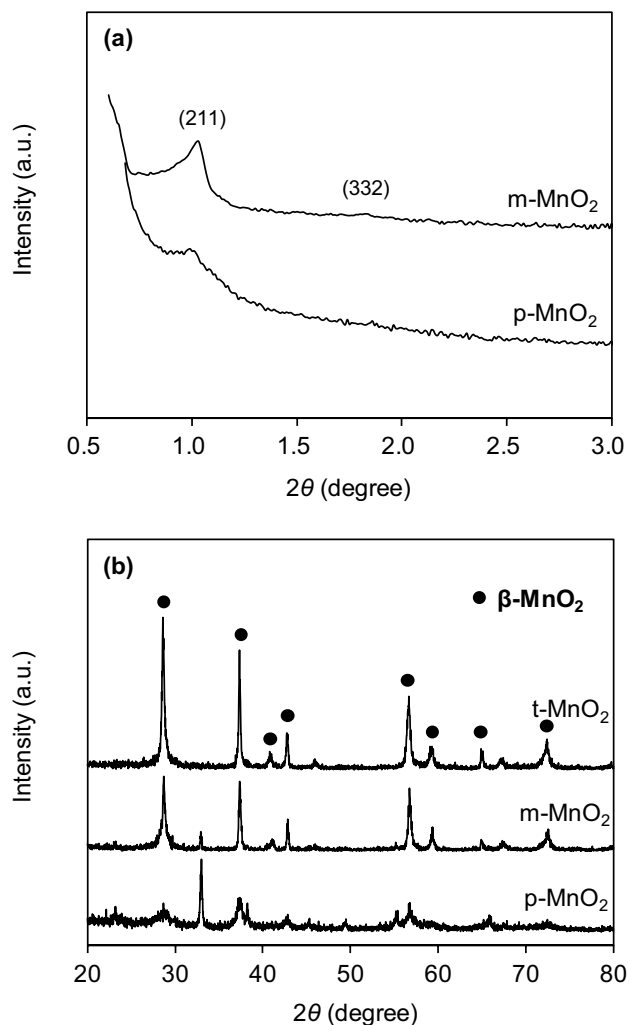


Fig. 1. (a) Small-angle and (b) wide-angle XRD patterns of the samples.

confirming that the mesoporous  $\text{MnO}_2$  structure was retained upon plasma modification.

The  $\text{N}_2$  adsorption-desorption isotherms and pore size distributions of the  $\text{MnO}_2$  adsorbents are displayed in Figs. 3a and b, respectively. The calculated structural parameters of the adsorbents are listed in Table 1. Both  $\text{m-MnO}_2$  and  $\text{p-MnO}_2$  (Fig. 3a) displayed well-defined type IV isotherms with hysteresis loops, indicative of the presence of mesostructured phases [30]. The specific surface area and pore volume of  $\text{m-MnO}_2$  were  $56.5 \text{ m}^2 \text{ g}^{-1}$  and  $0.16 \text{ cm}^3 \text{ g}^{-1}$ , respectively, which are superior to those obtained for  $\text{t-MnO}_2$  (Table 1). Such high specific surface areas and pore volumes would facilitate the adsorption and diffusion of  $\text{Pb(II)}$  and provide more active sites for  $\text{Pb(II)}$  adsorption. No difference in specific surface area or pore volume was observed after plasma modification. The pore sizes of  $\text{p-MnO}_2$  were 3.7 and 10.1 nm, which were identical to those of  $\text{m-MnO}_2$  (Fig. 3b). This result confirms that the porous structure of  $\text{m-MnO}_2$  remained unchanged upon plasma treatment.

The XPS spectra of  $\text{t-MnO}_2$ ,  $\text{m-MnO}_2$ , and  $\text{p-MnO}_2$  samples are presented in Fig. 4. The  $\text{Mn } 2\text{p}_{3/2}$  spectra of all adsorbents exhibited an asymmetric shape with numerous peaks (Fig. 4a), revealing a mixed-valence manganese system with  $\text{Mn}^{2+}$ ,  $\text{Mn}^{3+}$ , and  $\text{Mn}^{4+}$  species [5]. Due to the low  $\text{Mn}^{2+}$  contents in  $\text{MnO}_2$  materials, the  $\text{Mn } 2\text{p}_{3/2}$  spectra were deconvoluted into only two peaks at 640.7–641.2 and 642.2–642.7 eV, assigned to  $\text{Mn}^{3+}$  and  $\text{Mn}^{4+}$ , respectively [21]. The fitting parameters of the  $\text{Mn } 2\text{p}_{3/2}$  spectra are summarized in Table 2. The percentage of  $\text{Mn}^{4+}$  in  $\text{m-MnO}_2$  was higher than that in  $\text{t-MnO}_2$ , indicating that the mesoporous  $\text{MnO}_2$  sample exposed a higher amount of  $\text{Mn}^{4+}$  species on the surface, which may lead to an increased number of cationic vacancies and enhanced adsorption of heavy metal ions for the  $\text{Mn}^{3+}$  ions [5]. After plasma modification, the  $\text{Mn}^{4+}$  content on the mesoporous  $\text{MnO}_2$  surface decreased from 58.2% to 40.3%, which was attributed to the formation of additional complexation involving surface  $\text{Mn}^{4+}$  sites during the modification process.

The O 1s XPS spectra of  $\text{t-MnO}_2$ ,  $\text{m-MnO}_2$ , and  $\text{p-MnO}_2$  samples were highly asymmetrical (Fig. 4b) and could be deconvoluted into two peaks assigned to lattice and adsorbed oxygen, respectively [31]. The fitting parameters of the O 1s XPS spectra are listed in Table 2. The binding energies of lattice and adsorbed oxygen species ranged from 528.2 to 528.7 eV and from 530.2 to 530.9 eV, respectively. The content of lattice oxygen in  $\text{m-MnO}_2$  (63.0%) was higher than that of  $\text{t-MnO}_2$  (59.9%), which showed a significant shift to higher binding energies. This result confirms the formation of Mn-O-Mn bonds in  $\text{m-MnO}_2$ , due to the greater electron density of Mn-O-Mn than Mn-O-H groups [5]. The adsorbed oxygen fraction in  $\text{p-MnO}_2$  was 40.1%, much higher than that observed in  $\text{m-MnO}_2$  (37.0%; Table 2), reflecting an increase in adsorbed oxygen content after plasma modification. This result can be attributed to the formation of new Mn-O groups on the surface of the channels after the breaking of Mn-O-Mn bonds by oxygen radicals during plasma treatment.

The surface hydroxyl groups of the three  $\text{MnO}_2$  adsorbents were determined by the Boehm titration method [32]. The contents of surface hydroxyl groups on the  $\text{MnO}_2$  adsorbents are listed in Table 1. The hydroxyl group contents in  $\text{t-MnO}_2$ ,  $\text{m-MnO}_2$ , and  $\text{p-MnO}_2$  were 0.0045, 0.0409, and  $0.1091 \text{ mmol g}^{-1}$ , respectively. The hydroxyl group content of  $\text{m-MnO}_2$  was substantially higher than that of  $\text{t-MnO}_2$ , likely due to its larger specific surface area and more accessible pores. Moreover, the hydroxyl group content on the mesoporous  $\text{MnO}_2$  surface increased markedly after plasma modification, revealing that the modification was effective for generating a large number of hydroxyl groups on the surface of the channels.

The surface zeta potentials of  $\text{m-MnO}_2$  and  $\text{p-MnO}_2$  as a function of solution pH were studied and the results are shown in Fig. 5. The zeta potentials of the adsorbents monotonically decreased with increasing pH due to the continuous de-protonation of surface hydroxide groups. The isoelectric point (IEP) of  $\text{m-MnO}_2$  was 1.7. Notably, the much lower zeta potential was observed in  $\text{p-MnO}_2$  than in  $\text{m-MnO}_2$  in the test pH range of 1–10, and the IEP of  $\text{p-MnO}_2$  was calculated to be 1.4. The negative surface zeta potentials observed on  $\text{p-MnO}_2$  over a wide pH range suggested the potential for adsorptive removal of  $\text{Pb(II)}$  in water.

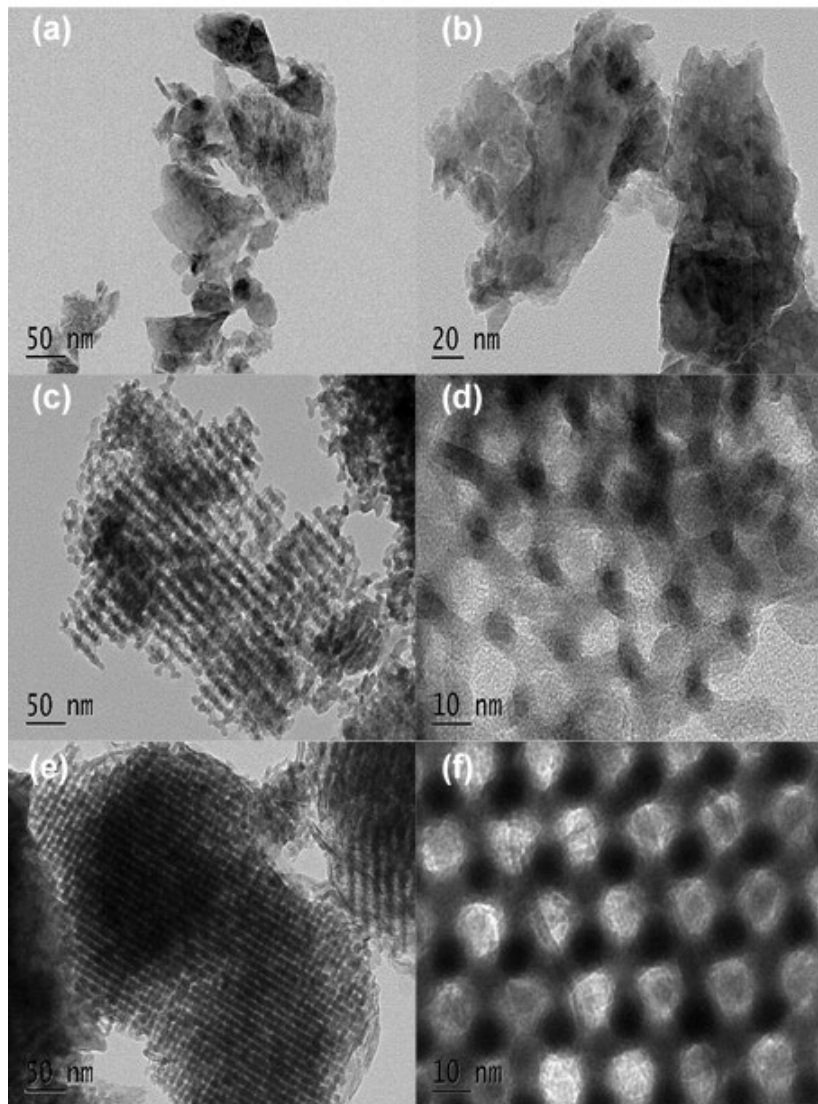


Fig. 2. TEM images of (a and b) t-MnO<sub>2</sub>, (c and d) m-MnO<sub>2</sub> and (e and f) p-MnO<sub>2</sub>.

### 3.2. Pb(II) adsorption dynamics

The effect of the agitation time on the Pb(II) adsorption by m-MnO<sub>2</sub> and p-MnO<sub>2</sub> is shown in Fig. 6a. The adsorption of Pb(II) by m-MnO<sub>2</sub> and p-MnO<sub>2</sub> was rapid within the first 60 min and reached equilibrium after 100 min. The adsorption rate constant was evaluated using the pseudo-first-order and pseudo-second-order rate expressions in Eqs. (2) and (3), respectively [21]:

$$\ln(q_e - q_t) = \ln q_e - k_1 t \quad (2)$$

$$\frac{t}{q_t} = \frac{1}{k_2 q_e^2} + \frac{t}{q_e} \quad (3)$$

where  $q_e$ ,  $q_t$ ,  $k_1$ , and  $k_2$  are the equilibrium adsorption capacity (mg g<sup>-1</sup>), the adsorption capacity (mg g<sup>-1</sup>) at time  $t$  (min), the pseudo-first-order rate constant (min<sup>-1</sup>), and

the pseudo-second-order rate constant (g mg<sup>-1</sup> min<sup>-1</sup>), respectively.

Fig. 6a displays the fitting curves obtained using the pseudo-first-order and pseudo-second-order models to describe the adsorption of Pb(II) on m-MnO<sub>2</sub> and p-MnO<sub>2</sub>. Table 3 lists the calculated kinetics parameters for Pb(II) adsorption on m-MnO<sub>2</sub> and p-MnO<sub>2</sub> obtained according to the equations. The correlation coefficients obtained for the pseudo-second-order model ( $R^2 > 0.99$ ) were higher than those of the pseudo-first-order model ( $R^2 > 0.93$ ), indicating that the pseudo-second-order model was more suitable for describing the kinetics of Pb(II) adsorption on m-MnO<sub>2</sub> and p-MnO<sub>2</sub>. Also, the equilibrium adsorption amounts ( $q_{cal}$ ) calculated for the pseudo-second-order kinetic model were very close to the experimental data ( $q_{exp}$ ), further confirming that the adsorption kinetics were well fitted by the pseudo-second-order kinetic model. The calculated pseudo-second-order rate constants for m-MnO<sub>2</sub> and p-MnO<sub>2</sub> were 0.0058 and 0.0027 g mg<sup>-1</sup> min<sup>-1</sup>, respectively. The adsorption rate

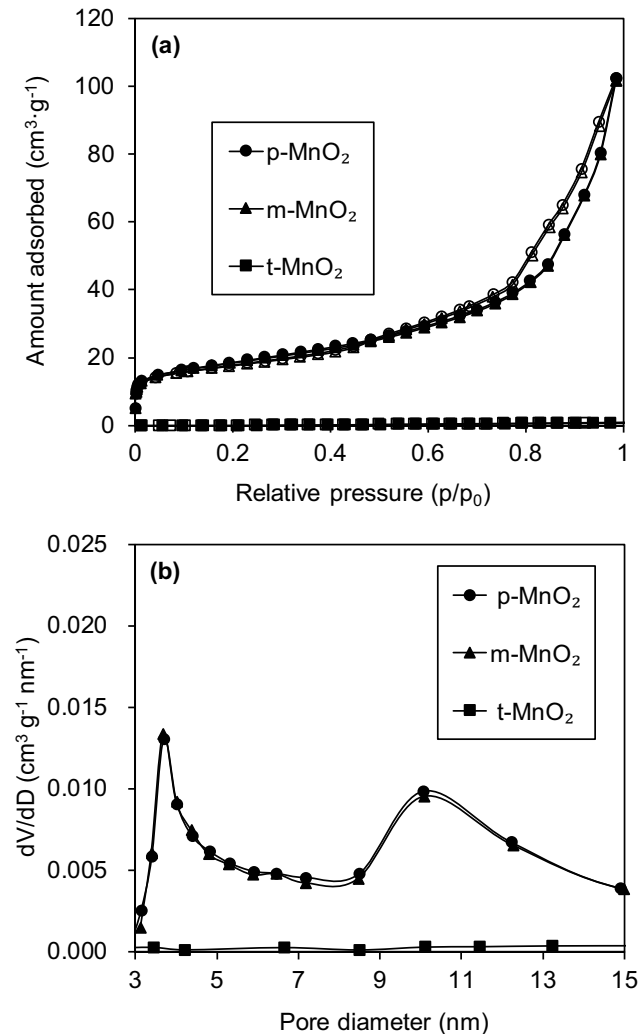


Fig. 3. (a) N<sub>2</sub> adsorption–desorption isotherms of t-MnO<sub>2</sub>, m-MnO<sub>2</sub> and p-MnO<sub>2</sub> and (b) pore size distributions of t-MnO<sub>2</sub>, m-MnO<sub>2</sub> and p-MnO<sub>2</sub>.

Table 1  
Structural properties of the adsorbents

| Sorbents           | $S_{\text{BET}}$<br>(m <sup>2</sup> g <sup>-1</sup> ) | $V_p^a$<br>(cm <sup>3</sup> g <sup>-1</sup> ) | $d_p^b$<br>(nm) | –OH <sup>c</sup><br>(mmol g <sup>-1</sup> ) |
|--------------------|---|---|-----------------|---|
| m-MnO <sub>2</sub> | 56.5  | 0.16  | 3.7/10.1        | 0.0409                                      |
| p-MnO <sub>2</sub> | 57.7  | 0.16  | 3.7/10.1        | 0.1091                                      |
| t-MnO <sub>2</sub> | 0.1   | —   | —               | 0.0045                                      |

<sup>a</sup>Total pore volume, determined at  $P/P_0 = 0.97$ .

<sup>b</sup>Most probable pore diameter, determined by BJH pore size distribution.

<sup>c</sup>Determined by Boehm titration method.

of m-MnO<sub>2</sub> was higher than that of p-MnO<sub>2</sub>, indicating that m-MnO<sub>2</sub> achieved the adsorption equilibrium faster.

Given that m-MnO<sub>2</sub> and p-MnO<sub>2</sub> are porous adsorbents, intraparticle diffusion may be an important factor in the adsorption process of Pb(II). Hence, the Weber–Morris

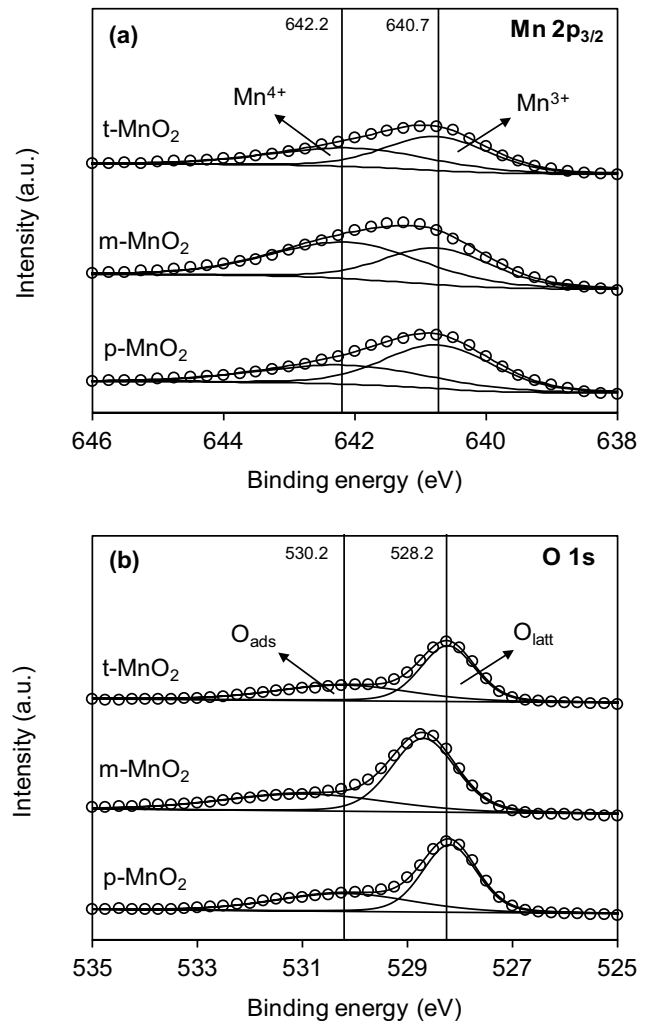


Fig. 4. (a) Mn 2p<sub>3/2</sub> and (b) O 1s XPS spectra of t-MnO<sub>2</sub>, m-MnO<sub>2</sub> and p-MnO<sub>2</sub>.

model, described by Eq. (4) [33], was applied to further investigate the Pb(II) adsorption process:

$$q_t = k_{\text{id}} t^{1/2} + C_i \quad (4)$$

where  $k_{\text{id}}$  (mg g<sup>-1</sup> min<sup>-1/2</sup>) is the intraparticle diffusion rate constant and  $C_i$  is the intercept of the  $q_t$  vs.  $t^{1/2}$  plot, which provides an estimate of the thickness of the boundary layer.

Fig. 6b displays the  $q_t$  vs.  $t^{1/2}$  plots for the adsorption of Pb(II) on m-MnO<sub>2</sub> and p-MnO<sub>2</sub>. The plots were multilinear, indicating that multiple adsorption steps were involved in the global adsorption processes. The  $q_t$  vs.  $t^{1/2}$  plots fitted using the linear regression method could be divided into three linear regions (Fig. 6b). The fitting parameters are summarized in Table 4. The initial, intermediate, and final linear regions were assigned to bulk diffusion, intraparticle diffusion, and adsorption equilibrium, respectively [34]. Moreover, the  $k_1$  values calculated from the slope of the first region of the plots for m-MnO<sub>2</sub> and p-MnO<sub>2</sub> were 24.94 and 35.43 mg g<sup>-1</sup> min<sup>-1/2</sup>, respectively, at the initial Pb(II) concentration of 50.0 mg L<sup>-1</sup>.

Table 2  
Results of XPS Mn 2p<sub>3/2</sub> and O 1s multiplets peak fitting

| Sorbents           | Mn <sup>3+</sup>        |                           |                         | Mn <sup>4+</sup> |              |            | O <sub>latt</sub> |              |            | OH <sub>ads</sub> |              |            |
|--------------------|-------------------------|---------------------------|-------------------------|------------------|--------------|------------|-------------------|--------------|------------|-------------------|--------------|------------|
|                    | BE <sup>a</sup><br>(eV) | FWHM <sup>b</sup><br>(eV) | At. <sup>c</sup><br>(%) | BE<br>(eV)       | FWHM<br>(eV) | At.<br>(%) | BE<br>(eV)        | FWHM<br>(eV) | At.<br>(%) | BE<br>(eV)        | FWHM<br>(eV) | At.<br>(%) |
| m-MnO <sub>2</sub> | 640.7                   | 1.93                      | 41.8                    | 642.1            | 2.70         | 58.2       | 528.7             | 1.45         | 63.0       | 530.9             | 3.66         | 37.0       |
| p-MnO <sub>2</sub> | 640.8                   | 2.04                      | 57.9                    | 642.2            | 2.81         | 42.1       | 528.2             | 1.22         | 59.9       | 530.2             | 3.06         | 40.1       |
| t-MnO <sub>2</sub> | 640.7                   | 1.85                      | 54.4                    | 642.1            | 2.84         | 45.6       | 528.2             | 1.22         | 59.9       | 530.2             | 3.00         | 40.1       |

<sup>a</sup>Binding energy.

<sup>b</sup>FWHM of all peaks was constrained.

<sup>c</sup>At. represents the percentage of the contribution for each peak to the total number of counts under the Mn 2p<sub>3/2</sub> or O 1s peak, and all peaks modeled as 70% Gaussian-30% Lorentzian.

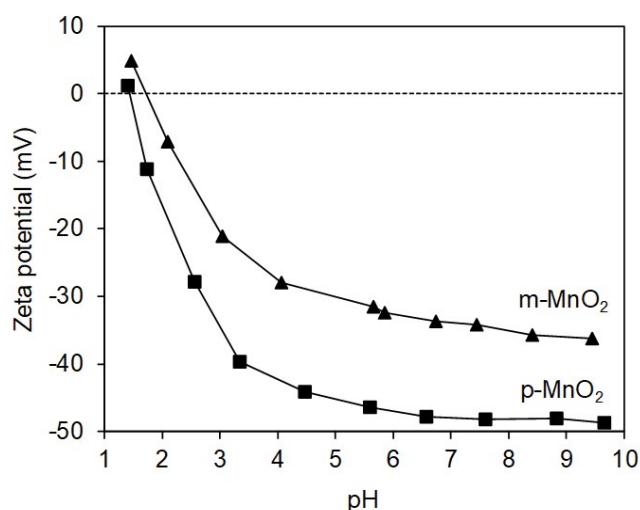


Fig. 5. Zeta potential of m-MnO<sub>2</sub> and p-MnO<sub>2</sub> as a function of pH.

The higher intraparticle diffusion rate of p-MnO<sub>2</sub> denotes an enhanced Pb(II) diffusion in mesoporous MnO<sub>2</sub> after plasma modification. Also, the greater C<sub>1</sub> value for m-MnO<sub>2</sub> is possibly due to a larger diffusion resistance, which led to a lower diffusion rate.

### 3.3. Pb(II) adsorption isotherms

The adsorption isotherms of Pb(II) on the MnO<sub>2</sub> adsorbents at 25°C are shown in Fig. 7a. The amount of Pb(II) adsorbed on m-MnO<sub>2</sub> was significantly higher than that on t-MnO<sub>2</sub> at the same equilibrium concentration, but lower than that adsorbed on p-MnO<sub>2</sub>, highlighting the enhanced adsorption capacity of mesoporous MnO<sub>2</sub> after plasma modification. The equilibrium data were fitted using the Freundlich and Langmuir isotherm models, described by Eqs. (5) and (6):

$$q_e = K_f C_e^{1/n} \quad (5)$$

$$q_e = \frac{q_m K_L C_e}{1 + K_L C_e} \quad (6)$$

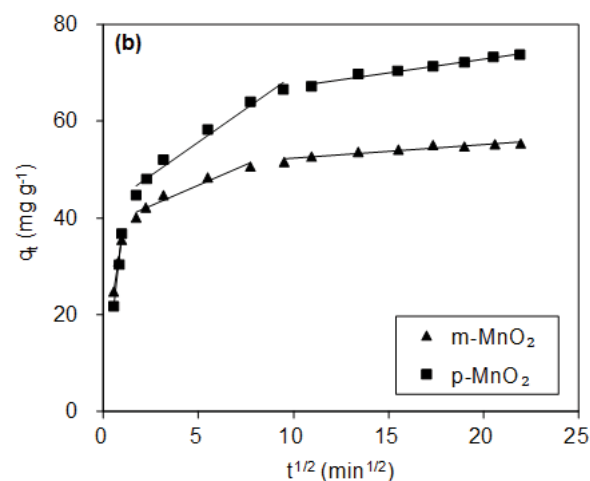
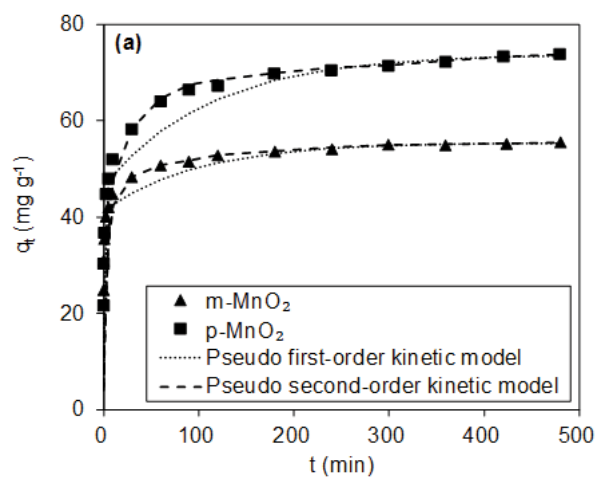


Fig. 6. Kinetics of Pb(II) adsorption onto m-MnO<sub>2</sub> and p-MnO<sub>2</sub>: (a) adsorption capacity vs. contact time and (b) the linear form of the Weber-Morris model.

where  $K_f$  and  $n$  are constants quantifying the adsorption capacity (mg g<sup>-1</sup>) and intensity, respectively, while  $q_m$ ,  $C_e$ , and  $K_L$  are the maximum adsorption capacity of the adsorbents (mg g<sup>-1</sup>), the equilibrium Pb(II) concentration (mg L<sup>-1</sup>), and the affinity constant (L mg<sup>-1</sup>), respectively.

Table 3  
Fitting parameters of Pb(II) adsorption kinetics using pseudo-first-order and pseudo-second-order model

| Sorbents           | Pseudo-first-order                 |                        |                                    |       | Pseudo-second-order                      |                                     |       |
|--------------------|------------------------------------|------------------------|------------------------------------|-------|--|-------------------------------------|-------|
|                    | $q_{\text{exp}} \text{ mg g}^{-1}$ | $k_1 \text{ min}^{-1}$ | $q_{\text{cal}} \text{ mg g}^{-1}$ | $R^2$ | $k_2 \text{ g mg}^{-1} \text{ min}^{-1}$ | $q'_{\text{cal}} \text{ mg g}^{-1}$ | $R^2$ |
| m-MnO <sub>2</sub> | 55.5                               | 0.0047                 | 54.1                               | 0.95  | 0.0058                                   | 55.5                                | 0.99  |
| p-MnO <sub>2</sub> | 73.8                               | 0.0031                 | 73.3                               | 0.92  | 0.0027                                   | 73.7                                | 0.99  |

Table 4  
Fitting parameters of Pb(II) adsorption kinetics using the Weber–Morris model

| Sorbents           | Weber–Morris model      |  |       |       |  |       |       |
|--------------------|-------------------------|--|-------|-------|--|-------|-------|
|                    | $C_0 \text{ mg L}^{-1}$ | $k_1 \text{ mg g}^{-1} \text{ min}^{-1/2}$ | $I_1$ | $R^2$ | $k_2 \text{ mg g}^{-1} \text{ min}^{-1/2}$ | $I_2$ | $R^2$ |
| m-MnO <sub>2</sub> | 50.0                    | 24.94                                      | 11.12 | 0.99  | 1.68                                       | 38.35 | 0.95  |
| p-MnO <sub>2</sub> | 50.0                    | 35.43                                      | 1.53  | 0.99  | 2.76                                       | 41.85 | 0.97  |

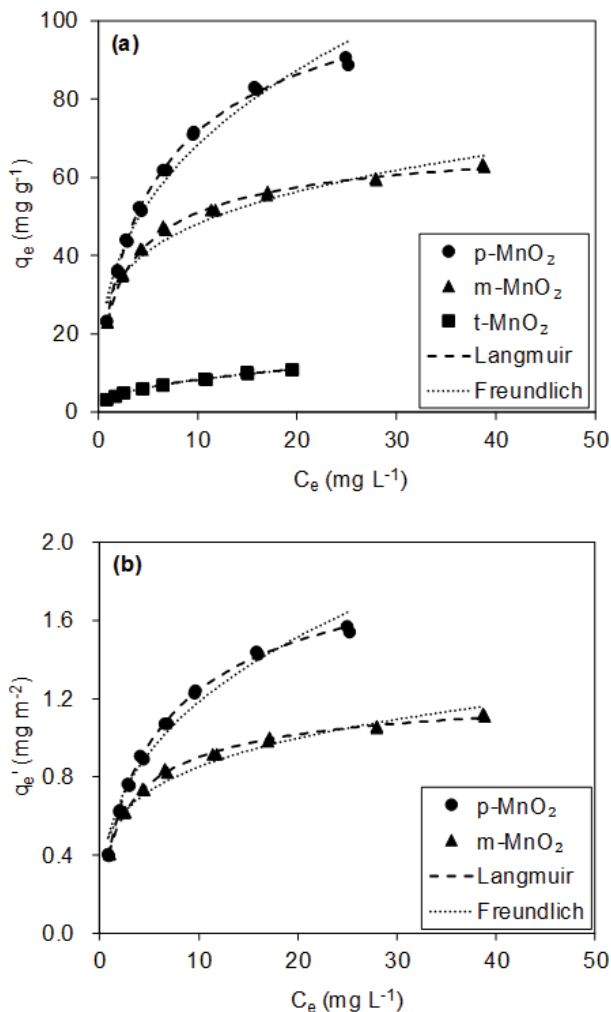


Fig. 7. (a) Pb(II) adsorption isotherms and (b) BET surface area normalized Pb(II) adsorption isotherms on the samples.

Table 5 lists the fitting parameters obtained from the Freundlich and Langmuir isotherm models. For t-MnO<sub>2</sub>, the correlation coefficient ( $R^2 > 0.997$ ) calculated from the Freundlich isotherm model was higher than that obtained with the Langmuir model ( $R^2 > 0.942$ ), suggesting that the Freundlich model provided a better description of the adsorption data. On the other hand, the adsorption isotherms of m-MnO<sub>2</sub> and p-MnO<sub>2</sub> were better fitted by the Langmuir ( $R^2 > 0.978$ ) than Freundlich ( $R^2 < 0.973$ ) model. These results indicate that the active sites for Pb(II) adsorption on the surface of m-MnO<sub>2</sub> and p-MnO<sub>2</sub> exhibited a more homogeneous distribution than those on the t-MnO<sub>2</sub> surface [10]. Also, the calculated maximum adsorption amount  $q_m$  and Freundlich coefficient  $K_f$  of m-MnO<sub>2</sub> were both higher than those of t-MnO<sub>2</sub> (Table 5), reflecting the enhanced Pb(II) adsorption capacity associated with the mesoporous structure of MnO<sub>2</sub>. The higher Pb(II) adsorption amount of m-MnO<sub>2</sub> is likely due to its uniform pore structure and high specific surface area, which improve the mass transfer and the exposure of active adsorption sites [35]. The  $q_m$  of p-MnO<sub>2</sub> obtained from the Langmuir model was 88.7 mg g<sup>-1</sup>, much higher than that of m-MnO<sub>2</sub> (59.9 mg g<sup>-1</sup>; Table 5).

To further evaluate the adsorption performance of m-MnO<sub>2</sub> and p-MnO<sub>2</sub>, the adsorption isotherms of the adsorbents were normalized by the specific surface area. Fig. 7b displays the normalized adsorption isotherms and Table 5 lists the normalized Pb(II) adsorption capacities of the adsorbents. The maximum normalized adsorption amounts of m-MnO<sub>2</sub> and p-MnO<sub>2</sub> were 1.12 and 1.75 mg m<sup>-2</sup>, respectively. The higher normalized adsorption capacity of p-MnO<sub>2</sub> was likely due to its higher adsorption site density, as a result of the increased number of hydroxyl groups in mesoporous MnO<sub>2</sub> after plasma modification.

After Pb(II) adsorption the p-MnO<sub>2</sub> adsorbent was further subjected to FT-IR analysis, and the results are shown in Fig. 8. One strong peak and a shoulder hump were observed at 620 and 3410 cm<sup>-1</sup> in FT-IR spectra are attributed to the stretching vibration of the Mn-O and -OH bonds, correspondingly [36–38]. It is necessary to mention here that the intensity of the -OH peak observed in the FT-IR spectra of

Table 5  
Fitting parameters of Pb(II) adsorption isotherms on the adsorbents using Langmuir and Freundlich isotherm models

| Sorbents           | Langmuir model              |                             |                              |       | Freundlich model            |      |       |
|--------------------|-----------------------------|-----------------------------|------------------------------|-------|-----------------------------|------|-------|
|                    | $K_L$ (L mg <sup>-1</sup> ) | $q_m$ (mg g <sup>-1</sup> ) | $q'_m$ (mg m <sup>-2</sup> ) | $R^2$ | $K_f$ (mg g <sup>-1</sup> ) | $n$  | $R^2$ |
| m-MnO <sub>2</sub> | 0.48                        | 63.4                        | 1.12                         | 0.978 | 28.4                        | 4.38 | 0.953 |
| p-MnO <sub>2</sub> | 0.27                        | 101.1                       | 1.75                         | 0.988 | 30.0                        | 2.80 | 0.973 |
| t-MnO <sub>2</sub> | 0.24                        | 12.4                        | —                            | 0.942 | 3.3                         | 2.47 | 0.997 |

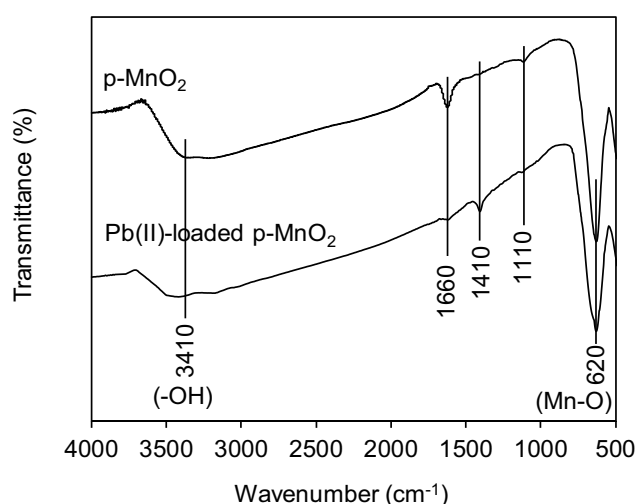


Fig. 8. FT-IR spectra of p-MnO<sub>2</sub> and p-MnO<sub>2</sub> after Pb(II) adsorption.

Pb-loaded p-MnO<sub>2</sub> is small. This could be probably due to the formation of Mn-O-Pb bonds in Pb(II)-loaded p-MnO<sub>2</sub> [10,21], and suggested that hydroxyl groups might be involved in metal ion uptake.

SEM images of p-MnO<sub>2</sub> and Pb(II)-loaded p-MnO<sub>2</sub> as well as their relevant elements mapping (O, Mn, and Pb) were also detected to confirm the adsorption mechanism, and the results depicted in Fig. 9. For p-MnO<sub>2</sub>, Pb element randomly distributed on its surface, while a large amount of Pb was dispersed closely on the surface of Pb(II)-loaded p-MnO<sub>2</sub> particles, reflecting a much higher Pb element content of Pb(II)-loaded p-MnO<sub>2</sub> than that of clean p-MnO<sub>2</sub>. Moreover, the element distribution of Pb in Fig. 9 was closely related to Mn and O distribution, suggesting that the Pb(II) uptake by p-MnO<sub>2</sub> was fully dominated by the Mn-OH sites [10].

The maximum monolayer adsorption capacities of m-MnO<sub>2</sub> and p-MnO<sub>2</sub> adsorbents for Pb(II) removal were compared with those of other adsorbents reported in the literature, and the values are shown in Table 6. It is clear from Table 6 that the p-MnO<sub>2</sub> adsorbent exhibited a much higher Pb(II) adsorption capacity than the previously reported adsorbents [21,39–42], which indicated that p-MnO<sub>2</sub> adsorbent is a promising adsorbent to remove Pb(II) from aqueous solutions.

### 3.4. Effect of solution pH on Pb(II) adsorption

The effect of the solution pH on Pb(II) adsorption on p-MnO<sub>2</sub> is shown in Fig. 10. The adsorbed amount of Pb(II)

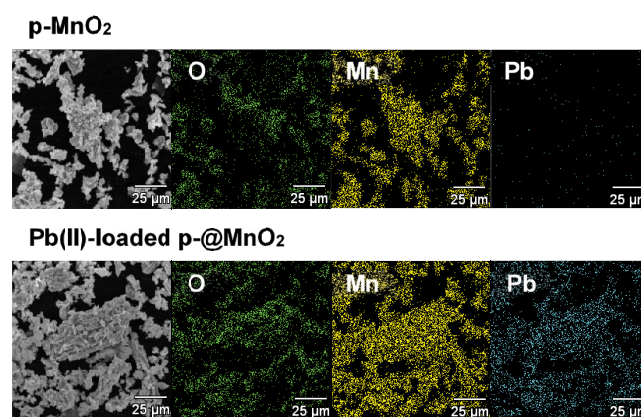


Fig. 9. SEM and elemental mapping images of p-MnO<sub>2</sub> and Pb(II)-loaded p-MnO<sub>2</sub>.

on p-MnO<sub>2</sub> increased monotonically in the pH range of 1–6 and stopped increasing above pH 6, which indicates that the adsorption process was pH-dependent. XPS and Boehm titration results revealed that hydroxyl groups were the main adsorption sites for Pb(II). Thus, the effect of the solution pH on the Pb(II) adsorption on p-MnO<sub>2</sub> was controlled by the protonation-deprotonation reaction of the surface hydroxyl groups [10]. The reported isoelectric point of β-MnO<sub>2</sub> is around 2 [43], and the p-MnO<sub>2</sub> surfaces are negatively charged at pH > 2. Hence, electrostatic attractive interactions are expected to occur between the negatively charged Mn-OH groups and the positive Pb(II) cations at a solution pH > 2. In other words, higher Pb(II) amounts are expected to be adsorbed at higher pH, and vice versa. However, Pb(II) adsorption was still observed on p-MnO<sub>2</sub> at pH < 2.0, likely due to the strong adsorption affinity of hydroxyl groups grafted on p-MnO<sub>2</sub> by plasma modification.

### 3.5. Effect of coexisting ions on Pb(II) adsorption

Industrial wastewater contains many coexisting ions, which may compete with Pb(II) for the active adsorption sites on the adsorbent surfaces. Here, the effects of different concentrations of coexisting Na<sup>+</sup> and Ca<sup>2+</sup> ions on the adsorption capacity of p-MnO<sub>2</sub> are presented in Fig. 11. The Pb(II) adsorption capacity of p-MnO<sub>2</sub> was higher in the presence than in the absence of coexisting ions, with Ca<sup>2+</sup> having a stronger influence than Na<sup>+</sup>. These results suggest a surface complexation-based mechanism for Pb(II) adsorption onto p-MnO<sub>2</sub> [44]. A similar adsorption mechanism for Pb(II)

Table 6  
Comparison of maximum monolayer adsorption capacities for Pb(II) removal

| Sorbents  | $q_m$<br>(mg g <sup>-1</sup> ) | $b$<br>(L mg <sup>-1</sup> ) | $R^2$ | Experimental conditions                 |     |         | References    |
|---|--------------------------------|------------------------------|-------|---|-----|---------|---------------|
|   |                                |                              |       | Sorbent dosage<br>(g mL <sup>-1</sup> ) | pH  | $T$ (K) |               |
| Al <sub>2</sub> O <sub>3</sub> -pillared layered MnO <sub>2</sub> | 87.7                           | 0.87                         | 0.925 | 0.5/1,000                               | 4.0 | 298     | [21]          |
| Polyethylene waste/nano-MnO <sub>2</sub>                          | 50.5                           | 1.78                         | 0.983 | 0.5/1,000                               | 5.0 | 295     | [39]          |
| Fe-Mn binary oxides-loaded biochar                                | 73.7                           | 0.32                         | 0.989 | 2.0/1,000                               | 4.0 | 298     | [40]          |
| Manganese oxide coated porous carbon                              | 40.6                           | 0.61                         | 0.993 | 1.0/1,000                               | 6.2 | 288     | [41]          |
| Amorphous manganese oxide   | 49.9                           | 2.38                         | 0.960 | 2.0/1,000                               | 4.0 | —       | [42]          |
| m-MnO <sub>2</sub>  | 63.4                           | 0.48                         | 0.978 | 0.5/1,000                               | 4.0 | 298     | Present study |
| p-MnO <sub>2</sub>  | 101.1                          | 0.27                         | 0.988 | 0.5/1,000                               | 4.0 | 298     | Present study |

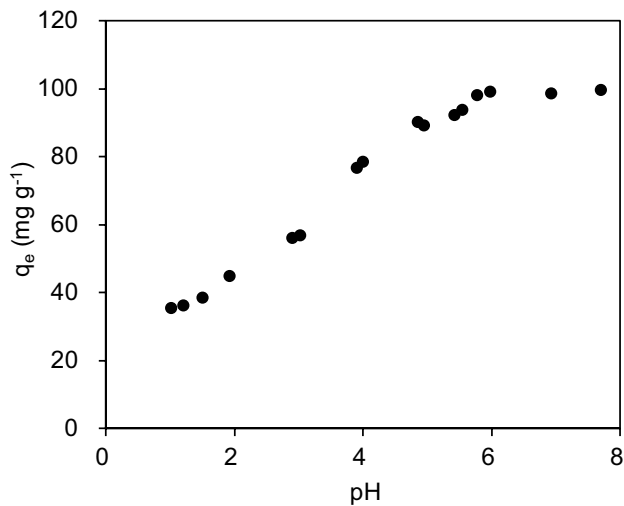


Fig. 10. Influence of solution pH on Pb(II) adsorption to p-MnO<sub>2</sub>.

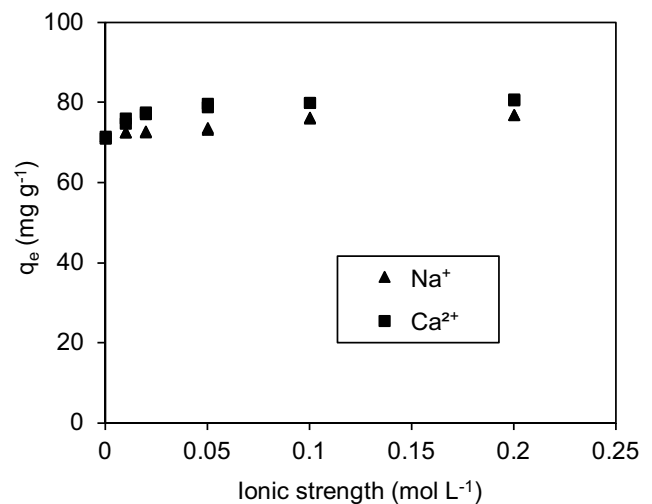


Fig. 11. Influence of co-existing ions (Na<sup>+</sup> and Ca<sup>2+</sup>) on Pb(II) adsorption to p-MnO<sub>2</sub>.

adsorption on manganese dioxide was reported in previous studies [45,46].

Copper (Cu(II)), nickel (Ni(II)) and zinc (Zn(II)) ions are commonly present in the industrial wastewater, and may affect the adsorption of Pb(II) onto sorbents. Experiments were carried out to investigate the adsorption performance of p-MnO<sub>2</sub> to Pb(II) in the presence of 0.01 mol L<sup>-1</sup> of Cu(II), Ni(II) and Zn(II), respectively, and the results are shown in Fig. 12. Obviously, the presence of Cu(II), Ni(II) or Zn(II) invoked a decrease of the adsorption for Pb(II) over p-MnO<sub>2</sub>. The decrease was possibly due to the competition between Pb(II) and coexisting ions for the surface hydroxyl groups of p-MnO<sub>2</sub>. Notably, p-MnO<sub>2</sub> still showed high adsorption capacities for Pb(II) in the presence of Cu(II), Ni(II) or Zn(II), further suggesting that the p-MnO<sub>2</sub> is capable of selectively adsorbing Pb(II) in wastewater.

### 3.6. Fixed-bed column sorption

A fixed-bed column sorption test of p-MnO<sub>2</sub> was conducted to investigate the potential of plasma-modified mesoporous MnO<sub>2</sub> for applications in engineering, and

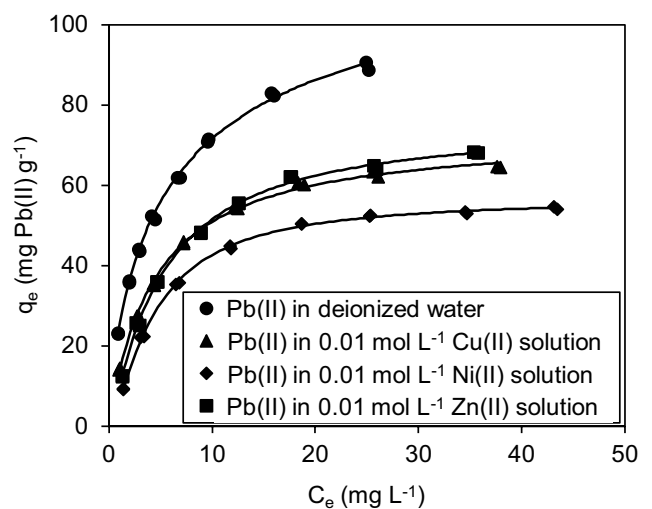


Fig. 12. Adsorption isotherms of p-MnO<sub>2</sub> to Pb(II) in the presence of 0.01 mol L<sup>-1</sup> of Cu(II), Ni(II) and Zn(II), respectively.

the breakthrough curve is shown in Fig. 13. The breakthrough point was set as  $0.1 \text{ mg L}^{-1}$  for Pb(II), as regulated maximum concentration level by China's quality standard for groundwater (GB/T 14848-2017). As can be seen in Fig. 13, the concentrations of Pb(II) in effluents maintained relatively lower in initial 170 min and then increased much faster. The p-MnO<sub>2</sub> sorbent exhibited a breakthrough point at the point of 730 min under the experimental conditions. The Thomas model was adopted to predict column sorption capacity (at  $C_d/C_0 = 1$ ), and the Thomas model is as Eq. (7) [21]:

$$\ln\left(\frac{C_{in}}{C_{out}} - 1\right) = \frac{k_{Th} q_m m}{Q} - k_{Th} C_{in} t \quad (7)$$

where  $C_{in}$  and  $C_{out}$  are the influent and effluent, respectively,  $k_{Th}$  is the Thomas rate constant ( $\text{ml min}^{-1} \text{mg}^{-1}$ ),  $q_m$  is the maximum adsorption capacity ( $\text{mg g}^{-1}$ ),  $Q$  is the flow rate ( $\text{mg min}^{-1}$ ),  $m$  is the mass of adsorbent (g), and  $t$  is the adsorption time (h). The removal capacity at the breakthrough point was  $4.4 \times 10^4 \text{ mg g}^{-1}$  for Pb(II), significantly higher than for commercial BCs, nano-MnO<sub>2</sub>, or MnO<sub>2</sub>-loaded resin [21,47,48]. This is mainly due to the highly dispersed MnO<sub>2</sub> on the surface of the BC. Therefore, p-MnO<sub>2</sub> is highly effective for removing heavy metals from water in fixed-bed and batch modes and is suitable for in situ environmental remediations.

A sample of wastewater from a Chinese electroplating plant in Yangzhou City was used as the influent to verify the feasibility of p-MnO<sub>2</sub> for decontaminating industrial wastewater. After treatment in a p-MnO<sub>2</sub> column for 10 h, the Pb(II) concentration in the effluent was  $0.013 \text{ mg L}^{-1}$ . The removal rate of total Pb(II) was >99.1%. Additionally, the pH and COD of the effluent were 5.23 and  $23.6 \text{ mg L}^{-1}$ , respectively. The pH of wastewater increased slightly, as reported for MnO<sub>2</sub> adsorbents for purifying electroplating wastewater [49,50]. The COD in effluent decreased by 97.3% compared to that in influent, suggesting that the p-MnO<sub>2</sub> column was also highly

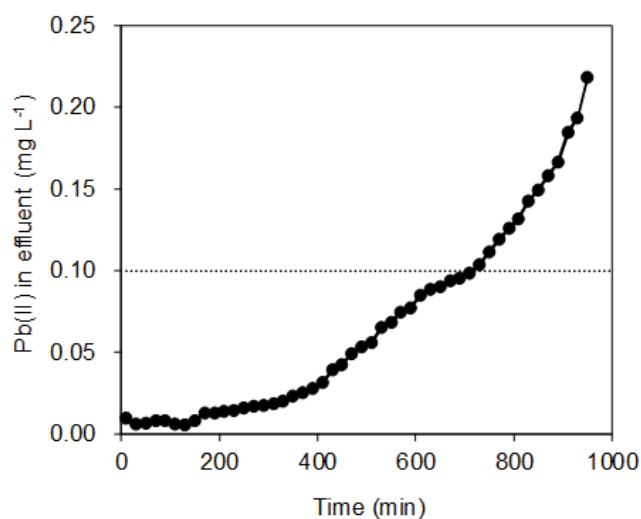


Fig. 13. Breakthrough curves for Pb(II) removal using p-MnO<sub>2</sub> adsorbents.

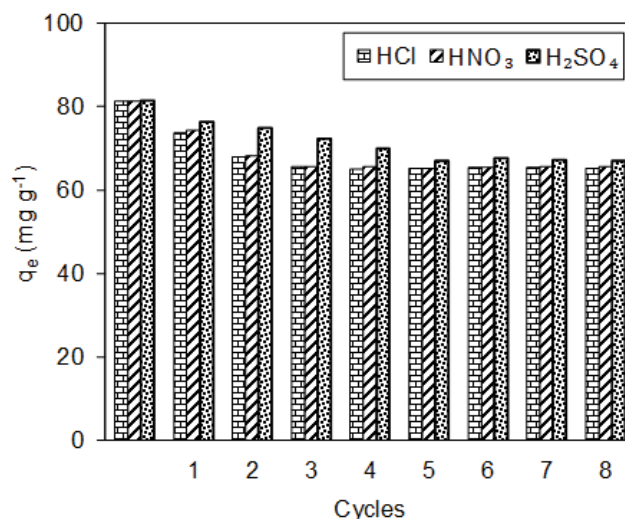


Fig. 14. Pb(II) adsorption to virgin and regenerated p-MnO<sub>2</sub> within eight adsorption-desorption cycles.

effective for the removal of COD from wastewater. Therefore, the p-MnO<sub>2</sub> column shows promise for remediation of electroplating wastewater in terms of removing Pb(II).

### 3.7. Adsorbent reusability

The reusability of an adsorbent is of crucial importance for its practical applications. Because of the low Pb(II) adsorption capacity at low pH (Fig. 14), the adsorbed Pb(II) on the p-MnO<sub>2</sub> adsorbent was eluted using  $0.1 \text{ mol L}^{-1}$  HCl, HNO<sub>3</sub> and H<sub>2</sub>SO<sub>4</sub> solution, respectively. The regenerated p-MnO<sub>2</sub> was employed in repeated Pb(II) adsorption tests. After three adsorption-desorption cycles, the decrease in Pb(II) adsorption capacity was calculated to be 19.4%, 19.5%, and 11.3% by using HCl, HNO<sub>3</sub>, and H<sub>2</sub>SO<sub>4</sub> as desorption agent, respectively. The higher desorption efficiency of H<sub>2</sub>SO<sub>4</sub> is likely due to the higher concentration of hydrogen ions, resulting in stronger competition between hydrogen ions and adsorbed Pb(II) on p-MnO<sub>2</sub> surfaces. The Pb(II) adsorption remained constant within the next five adsorption-desorption cycles (Fig. 14), suggesting that p-MnO<sub>2</sub> could be used repeatedly as a highly stable adsorbent for Pb(II) removal from aqueous solutions.

## 4. Conclusions

In the current study, we prepared a mesoporous MnO<sub>2</sub> (m-MnO<sub>2</sub>) material and modified it by plasma treatment (p-MnO<sub>2</sub>) for the adsorptive removal of Pb(II) from aqueous solutions. The characterization experiments showed that the mesoporous structure of the adsorbent was barely affected by the plasma treatment, whereas the number of surface hydroxyl groups increased considerably. Compared to m-MnO<sub>2</sub>, p-MnO<sub>2</sub> exhibited a higher adsorption capacity for Pb(II) and showed a maximum Pb(II) capacity of  $88.7 \text{ mg g}^{-1}$ . The improved adsorption capacity of p-MnO<sub>2</sub> is likely due to the large number of hydroxyl groups generated on the adsorbent surfaces by plasma modification. Also, p-MnO<sub>2</sub> showed a high working adsorption capacity in the column

test. The present results indicate that plasma-modified mesoporous MnO<sub>2</sub> is a highly effective and reusable adsorbent for Pb(II) from aqueous solutions.

### Acknowledgments

This work was supported by the National Natural Science Foundation of China (grant numbers 31901447, 41701329 and 41701093), the Jiangsu Natural Science Foundation (grant number BK20160468), and the China Postdoctoral Science Foundation (Grant number 2019M651979). The authors would like to thank the Testing Center of Yangzhou University for support with the material characterization experiments.

### References

- [1] S. Brown, R. Chaney, J. Hallfrisch, Q. Xue, Effect of biosolids processing on lead bioavailability in an urban soil, *J. Environ. Qual.*, 32 (2003) 100–108.
- [2] K. Jomova, M. Valko, Advances in metal-induced oxidative stress and human disease, *Toxicology*, 283 (2011) 65–87.
- [3] L. Guo, L. Liu, M. Zhuo, S. Fu, Y. Xu, W. Zhou, C. Shi, B. Ye, Y. Li, W. Chen, Small-lateral-size graphene oxide hydrosols sealed in dialysis bags for enhanced trace Pb(II) removal from water without re-pollution, *Appl. Surf. Sci.*, 445 (2018) 586–595.
- [4] X. Meng, H.J. Wang, D. Lei, D. Qu, Y.J. Zhai, Y.L. Wang, Removal of Pb(II) from aqueous solution by hydrous manganese dioxide: adsorption behavior and mechanism, *J. Environ. Sci.*, 25 (2013) 479–486.
- [5] Y. Wang, X. Feng, M. Villalobos, W. Tan, F. Liu, Sorption behavior of heavy metals on birnessite: relationship with its Mn average oxidation state and implications for types of sorption sites, *Chem. Geol.*, 292–293 (2012) 25–34.
- [6] C.X. He, F.C. Xie, Adsorption behavior of manganese dioxide towards heavy metal ions: surface zeta potential effect, *Water Air Soil Pollut.*, 229 (2018) 77.
- [7] S.M. Maliyekkal, K.P. Lisha, T. Pradeep, A novel cellulose-manganese oxide hybrid material by in situ soft chemical synthesis and its application for the removal of Pb(II) from water, *J. Hazard. Mater.*, 181 (2010) 986–995.
- [8] S. Mallakpour, F. Motirasoul, Covalent surface modification of  $\alpha$ -MnO<sub>2</sub> nanorods with L-valine amino acid by solvothermal strategy, preparation of PVA/ $\alpha$ -MnO<sub>2</sub>-L-valine nanocomposite films and study of their morphology, thermal, mechanical, Pb(II) and Cd(II) adsorption properties, *RSC Adv.*, 6 (2016) 62602–62611.
- [9] Q.X. Zhang, H. Wen, D. Peng, X.J. Huang, Interesting interference evidence of electrochemical detection of Zn(II), Cd(II) and Pb(II) on three different morphologies of MnO<sub>2</sub> nanocrystals, *J. Electroanal. Chem.*, 739 (2015) 89–96.
- [10] H.P. Zhang, A.B. Wu, H.Y. Fu, L. Zhang, H. Liu, S.R. Zheng, H.Q. Wan, Z.Y. Xu, Efficient removal of Pb(II) ions using manganese oxides: the role of crystal structure, *RSC Adv.*, 7 (2017) 41228–41240.
- [11] S. Bag, C.R. Raj, Hierarchical three-dimensional mesoporous MnO<sub>2</sub> nanostructures for high performance aqueous asymmetric supercapacitors, *J. Mater. Chem. A*, 4 (2016) 587–595.
- [12] S.M. Sun, W.Z. Wang, M. Shang, J. Ren, L. Zhang, Efficient catalytic oxidation of tetraethylated rhodamine over-ordered mesoporous manganese oxide, *J. Mol. Catal. A: Chem.*, 320 (2010) 72–78.
- [13] B. Zhi, H. Ding, D.M. Wang, Y. Cao, Y. Zhang, X. Wang, Y.L. Liu, Q.S. Huo, Ordered mesoporous MnO<sub>2</sub> as a synergetic adsorbent for effective arsenic(III) removal, *J. Mater. Chem. A*, 2 (2014) 2374–2382.
- [14] X.G. Wang, K.S.K. Lin, J.C.C. Chan, S. Cheng, Direct synthesis and catalytic applications of ordered large pore aminopropyl-functionalized SBA-15 mesoporous materials, *J. Phys. Chem. B*, 109 (2005) 1763–1769.
- [15] Y.J. Yang, J.J. Wang, X.Q. Qian, Y.H. Shan, H.P. Zhang, Aminopropyl-functionalized mesoporous carbon (APTMS-CMK-3) as effective phosphate adsorbent, *Appl. Surf. Sci.*, 427 (2018) 206–214.
- [16] M. Kundu, C.C. Albert Ng, D.Y. Petrovykh, L.F. Liu, Nickel foam supported mesoporous MnO<sub>2</sub> nanosheet arrays with superior lithium storage performance, *Chem. Commun.*, 49 (2013) 8459–8461.
- [17] J.P. Ma, Q.L. Cheng, V. Pavlinek, P. Saha, C.Z. Li, Morphology-controllable synthesis of MnO<sub>2</sub> hollow nanospheres and their supercapacitive performance, *New J. Chem.*, 37 (2013) 722–728.
- [18] R.A. Chandru, S. Patra, C. Oommen, N. Munichandraiah, B.N. Raghunandan, Exceptional activity of mesoporous  $\beta$ -MnO<sub>2</sub> in the catalytic thermal sensitization of ammonium perchlorate, *J. Mater. Chem.*, 22 (2012) 6536–6538.
- [19] F. Kleitz, S.H. Choi, R. Ryoo, Cubic Ia3d large mesoporous silica: synthesis and replication to platinum nanowires, carbon nanorods and carbon nanotubes, *Chem. Commun.*, 9 (2003) 2136–2137.
- [20] J.Y. Luo, J.J. Zhang, Y.Y. Xia, Highly electrochemical reaction of lithium in the ordered mesoporous  $\beta$ -MnO<sub>2</sub>, *Chem. Mater.*, 18 (2006) 5618–5623.
- [21] H.P. Zhang, L.Q. Gu, L. Zhang, S.R. Zheng, H.Q. Wan, J.Y. Sun, D.Q. Zhu, Z.Y. Xu, Removal of aqueous Pb(II) by adsorption on Al<sub>2</sub>O<sub>3</sub>-pillared layered MnO<sub>2</sub>, *Appl. Surf. Sci.*, 406 (2017) 330–338.
- [22] J. Gao, X. Zhu, Z.J. Bian, T. Jin, J. Hu, H.L. Liu, Paving the way for surface modification in one-dimensional channels of mesoporous materials via plasma treatment, *Microporous Mesoporous Mater.*, 202 (2015) 16–21.
- [23] F. Mattelaer, P.M. Vereecken, J. Dendooven, C. Detavernier, Deposition of MnO anode and MnO<sub>2</sub> cathode thin films by plasma-enhanced atomic layer deposition using the Mn(thd)<sub>3</sub> precursor, *Chem. Mater.*, 27 (2015) 3628–3635.
- [24] J.H. Bang, K.S. Suslick, Applications of ultrasound to the synthesis of nanostructured materials, *Adv. Mater.*, 22 (2010) 1039–1059.
- [25] N. Fang, D.J. Xi, J.Y. Xu, M. Ambati, W. Srituravanich, C. Sun, X. Zhang, Ultrasonic metamaterials with negative modulus, *Nat. Mater.*, 5 (2006) 452–456.
- [26] Y.X. Liu, H.X. Dai, J.G. Deng, S.H. Xie, H.G. Yang, W. Tan, W. Han, Y. Jiang, G.S. Guo, Mesoporous Co<sub>3</sub>O<sub>4</sub>-supported gold nanocatalysts: highly active for the oxidation of carbon monoxide, benzene, toluene, and o-xylene, *J. Catal.*, 309 (2014) 408–418.
- [27] B.Y. Bai, J.H. Li, J.M. Hao, 1D-MnO<sub>2</sub>, 2D-MnO<sub>2</sub> and 3D-MnO<sub>2</sub> for low-temperature oxidation of ethanol, *Appl. Catal., B*, 164 (2015) 241–250.
- [28] L.X. Li, P. Hua, X.K. Tian, C. Yang, Z.B. Pi, Synthesis and electrochemical properties of two types of highly ordered mesoporous MnO<sub>2</sub>, *Electrochim. Acta*, 55 (2010) 1682–1686.
- [29] F. Jiao, P.G. Bruce, Mesoporous crystalline  $\beta$ -MnO<sub>2</sub>: a reversible positive electrode for rechargeable lithium batteries, *Adv. Mater.*, 19 (2007) 657–660.
- [30] W. Xiao, W.J. Zhou, H. Yu, Y. Pu, Y.H. Zhang, C.B. Hu, Template synthesis of hierarchical mesoporous MnO<sub>2</sub> hollow microspheres as electrode material for high-performance symmetric supercapacitor, *Electrochim. Acta*, 264 (2018) 1–11.
- [31] J. Zhang, Y. Cao, C. Wang, R. Ran, Design and preparation of MnO<sub>2</sub>/CeO<sub>2</sub>-MnO<sub>2</sub> double-shelled binary oxide hollow spheres and their application in CO oxidation, *ACS Appl. Mater. Interfaces*, 8 (2016) 8670–8677.
- [32] H.P. Boehm, Some aspects of the surface chemistry of carbon blacks and other carbons, *Carbon*, 32 (1994) 759–769.
- [33] W.J. Weber, J.C. Morris, Kinetics of adsorption on carbon from solution, *J. Sanit. Eng. Div.*, 89 (1963) 31–60.
- [34] S. Mohan, V. Kumar, D.K. Singh, S.H. Hasan, Effective removal of lead ions using graphene oxide-MgO nanohybrid from aqueous solution: isotherm, kinetic and thermodynamic modeling of adsorption, *J. Environ. Chem. Eng.*, 5 (2017) 2259–2273.
- [35] A.B. Diciara, M.R. Webber, W.R. Gorman, R.E. Rogers, Removal of copper ions from aqueous solutions via adsorption on carbon nanocomposites, *ACS Appl. Mater. Interfaces*, 7 (2015) 15674–15680.

- [36] P.M. Ette, K. Selvakumar, S.M.S. Kumar, K. Ramesha, Silica template-assisted synthesis of ordered mesoporous  $\beta$ - $\text{MnO}_2$  nanostructures and their performance evaluation as a negative electrode in Li-ion batteries, *Electrochim. Acta*, 292 (2018) 532–539.
- [37] R.Z. Xie, W.J. Jiang, L. Wang, J.F. Peng, Y. Chen, Effect of pyrolusite loading on sewage sludge-based active carbon in Cu(II), Pb(II), and Cd(II) adsorption, *Environ. Prog. Sustainable Energy*, 32(2013) 1066–1073.
- [38] R.P.D. Victor, L.L.M. Fontes, A.A. Neves, M.E.L.R. de Queiroz, A.F. de Oliveira, L.D.L. Miranda, Removal of orange G dye by manganese oxide nanostructures, *J. Braz. Chem. Soc.*, 30 (2019) 1769–1778.
- [39] A.G. Al Lafi, J. Al Abdullah, T. Alnama, Y. Amin, Removal of lead from aqueous solution by polyethylene waste/nano-manganese dioxide composite, *J. Polym. Environ.*, 25 (2017) 391–401.
- [40] L.K. Zhang, X.Y. Liu, X.M. Huang, W.D. Wang, P. Sun, Y.M. Li, Adsorption of  $\text{Pb}^{2+}$  from aqueous solutions using Fe-Mn binary oxides-loaded biochar: kinetics, isotherm, and thermodynamic studies, *Environ. Technol.*, 40 (2019) 1853–1861.
- [41] G.Q. Tan, Y. Liu, D. Xiao, Preparation of manganese oxides coated porous carbon and its application for lead ion removal, *Carbohydr. Polym.*, 219 (2019) 306–315.
- [42] L.D. Puppa, M. Komárek, F. Bordas, J.C. Bollinger, E. Joussein, Adsorption of copper, cadmium, lead and zinc onto a synthetic manganese oxide, *J. Colloid Interface Sci.*, 399 (2013) 99–106.
- [43] J.W. Tokin, L.S. Balistrieri, J.W. Murray, Modeling sorption of divalent metal cations on hydrous manganese oxide using the diffuse double layer model, *Appl. Geochem.*, 19 (2004) 29–53.
- [44] E. Kim, C. Lee, Y.Y. Chang, Y.S. Chang, Hierarchically structured manganese oxide-coated magnetic nanocomposites for the efficient removal of heavy metal ions from aqueous systems, *ACS Appl. Mater. Interfaces*, 5 (2013) 9628–9634.
- [45] Y.Z. Li, R. Zhao, S. Chao, B.L. Sun, C. Wang, X. Li, Polydopamine coating assisted synthesis of  $\text{MnO}_2$  loaded inorganic/organic composite electrospun fiber adsorbent for efficient removal of  $\text{Pb}^{2+}$  from water, *Chem. Eng. J.*, 344 (2018) 277–289.
- [46] X. Wang, K. Huang, Y. Chen, J.F. Liu, S. Chen, J.L. Cao, S.R. Mei, Y.K. Zhou, T. Jing, Preparation of dumbbell manganese dioxide/gelatin composites and their application in the removal of lead and cadmium ions, *J. Hazard. Mater.*, 350 (2018) 46–54.
- [47] L.J. Dong, Z.L. Zhu, H.M. Ma, Y.L. Qiu, J.F. Zhao, Simultaneous adsorption of lead and cadmium on  $\text{MnO}_2$ -loaded resin, *J. Environ. Sci.*, 22 (2010) 225–229.
- [48] J. Ifthikar, X. Jiao, A. Ngambia, T. Wang, A. Khan, A. Jawad, Q. Xue, L. Liu, Z.Q. Chen, Facile one-pot synthesis of sustainable carboxymethyl chitosan-sewage sludge biochar for effective heavy metal chelation and regeneration, *Bioresour. Technol.*, 262 (2018) 22–31.
- [49] G.Q. Tan, Y. Wu, Y. Liu, D. Xiao, Removal of Pb(II) ions from aqueous solution by manganese oxide coated rice straw biochar- a low-cost and highly effective sorbent, *J. Taiwan Inst. Chem. Eng.*, 84 (2018) 85–92.
- [50] H.J. Xie, Y.X. Yang, J.H. Liu, Y. Kang, J. Zhang, Z. Hu, S. Liang, Enhanced triclosan and nutrient removal performance in vertical up-flow constructed wetlands with manganese oxides, *Water Res.*, 143 (2018) 457–466.